

## ORIGINAL ARTICLE

# Potential of combined neutron and X-ray imaging to quantify local carbon contents in soil

John Koestel<sup>1,2</sup>  | Jumpei Fukumasu<sup>1</sup>  | Mats Larsbo<sup>1</sup> |  
Anke M. Herrmann<sup>1</sup> | Pawala Ariyathilaka<sup>3</sup> | Oxana V. Magdysyuk<sup>4</sup> |  
Geneveva Burca<sup>5,6</sup> 

<sup>1</sup>Department of Soil and Environment, Swedish University of Agricultural Sciences, Uppsala, Sweden

<sup>2</sup>Soil Fertility and Soil Protection, Agroscope Reckenholz-Tanikon, Zürich, Switzerland

<sup>3</sup>Scitech Precision Limited, Rutherford Appleton Laboratory, Didcot, UK

<sup>4</sup>Diamond Light Source, Rutherford Appleton Laboratory, Didcot, UK

<sup>5</sup>ISIS Pulsed Neutron and Muon Source, Rutherford Appleton Laboratory, Didcot, UK

<sup>6</sup>Faculty of Science and Engineering, University of Manchester, Manchester, UK

## Correspondence

John Koestel, Department of Soil and Environment, Swedish University of Agricultural Sciences, Box 7014, 750 07 Uppsala, Sweden.  
Email: john.koestel@slu.se

## Funding information

Open access funding provided by Agroscope.

## Abstract

In this study, we investigated the potential and limitations of using joint X-ray and time-of-flight (TOF) neutron imaging for mapping the 3-dimensional organic carbon distribution in soil. This approach is viable because neutron and X-ray beams have complementary attenuation properties. Soil minerals consist to a large part of silicon and aluminium, and elements that are relatively translucent to neutrons but attenuate X-rays. In contrast, attenuation of neutrons is strong for hydrogen, which is abundant in soil organic matter (SOM), while hydrogen barely attenuates X-rays. In theory, TOF neutron imaging does further more allow the imaging of Bragg edges, which correspond to d-spacings in minerals. This could help to distinguish between SOM and clay minerals, the mineral group in soil that is most strongly associated with hydrogen atoms. We collected TOF neutron image data at the IMAT beamline at the ISIS facility and synchrotron X-ray image data at the I12 beamline at the Diamond Light source, both located within the Rutherford Appleton Laboratory, Harwell, UK. The white beam (the full energy spectrum) neutron image clearly showed variations in neutron attenuation within soil aggregates at approximately constant X-ray attenuations. This indicates a constant bulk density with varying organic matter and/or clay content. Unfortunately, the combination of TOF neutron and X-ray imaging was not suited to allow for a distinction between SOM and clay minerals at the voxel scale. While such a distinction is possible in theory, it is prevented by technical limitations. One of the main reasons is that the neutron frequencies available at modern neutron sources are too large to capture the main d-spacings of clay minerals. As a result, inference to voxel scale SOM concentrations is presently not feasible. Future improved neutron sources and advanced detector designs will eventually overcome the technical problems encountered here. On the positive side, combined X-ray and TOF neutron imaging demonstrated abilities to identify quartz grains and to distinguish between plastics and plant seeds.

This is an open access article under the terms of the Creative Commons Attribution-NonCommercial License, which permits use, distribution and reproduction in any medium, provided the original work is properly cited and is not used for commercial purposes.

© 2021 The Authors. *European Journal of Soil Science* published by John Wiley & Sons Ltd on behalf of British Society of Soil Science.

### Highlights

- Full understanding of biogeochemical processes requires three-dimensional (3-D) maps of organic matter in soil (SOM).
- This study investigates a novel method to map voxel-scale SOM contents with 3-D resolution.
- The method is based a combination of X-ray and time-of-flight neutron tomography.
- At present, technical limitations prevent distinguishing between SOM and clay mineral contents.
- More advanced neutron sources are required to overcome the encountered technical obstacles.

### KEYWORDS

correlative imaging, neutron imaging, soil organic matter, soil structure, X-ray imaging

## 1 | INTRODUCTION

The interplay among soil structure, soil organic matter (SOM) and soil biota is fundamental for the terrestrial carbon cycle, its turnover and impact on future climate. Despite decades of research on the carbon cycle in soil, quantitative descriptions of microbiological activity in soils and the associated fate of carbon remains a challenge (Baveye et al., 2018). This shortcoming is linked to a knowledge gap of how the complex soil pore structure and respective distribution of organic carbon shape the soil biota and its activity (Nunan et al., 2020). One major obstacle to arrive at models with an improved description of the carbon cycle in soil is the general lack of relevant experimental data that may inform the development of such models and their validation (Baveye et al., 2018). More specifically, a method that allows reliable three-dimensional mapping of organic matter in intact soil at scales larger than a few millimetres is missing.

During recent years, significant progress has been made in quantifying the morphology and topology of soil pore systems using X-ray tomography, a non-invasive, three-dimensional (3-D) imaging method (Cnudde & Boone, 2013; Wildenschild & Sheppard, 2013). X-ray imaging can also be used to identify organic objects that are larger than the image resolution (Koestel, 2018). In contrast, it is not possible to quantify the distribution of SOM and microbes smaller than the image resolution from X-ray images only. This is typically the case for microbes and for smaller chunks of particulate organic matter and material associated with soil minerals at the molecular level. To investigate microbes and SOM at smaller scales, commonly, thin sections are created

where two-dimensional (2-D) cross-sections of the investigated soil volume are exposed. Then, for example, hot-spots for microbial activity can be investigated using zymography (Spohn et al., 2013). A link between microbial activity and soil structure can then be gained by combining zymography with X-ray imaging (Kravchenko et al., 2019). A 3-D distribution may be obtained by applying staining repeatedly after consecutively removing slices of the soil. The resulting spatial resolution is, however, poor. A finer resolution is achieved when the soil is first fixed by embedding it in resin, so that the layer thickness can be reduced and the surface can be polished. Using this method, the location of microorganisms is visualised, for example, by fluorescence in situ hybridisation (Eickhorst & Tippkötter, 2008). Again, a coupling to the pore space may be achieved when the method is combined with X-ray imaging (Schlüter et al., 2019). Yet, a drawback of this method is that all resins contain carbon, making them unsuitable when the goal is to map organic carbon concentrations. Nano-SIMS (Nanoscale Secondary Ion Mass Spectrometry) offers a solution to this problem as it allows measurements of isotopic compositions. It is therefore possible to distinguish between autochthonous carbon and carbon in the resin provided that their isotopic signatures are different (Herrmann et al., 2007). However, Nano-SIMS is restricted to spatial scales of less than a few 100  $\mu\text{m}$ . Another alternative is to map soil carbon concentrations by osmium staining, as outlined in Peth et al. (2014), Rawlins et al. (2016) and Arai et al. (2019). Due to the osmium's strong adsorption to organic matter and its large atomic number, it is possible to image osmium concentration from dual-energy 3-D synchrotron X-ray images. Major drawbacks to this method are the toxicity of  $\text{OsO}_4$  and the fact that  $\text{OsO}_4$  only stains a small

fraction of the SOM, and it does not stain all types of organic material equally well (Zheng et al., 2020).

Recent developments in neutron and X-ray imaging have the potential to quantify organic matter concentrations in soil without staining. This possibility arises due to the complementary sensitivities of these imaging methods. An illustration of the basic principle of this approach is shown in Kaestner et al. (2017). The attenuation of X-rays with photon energies above 50 keV is approximately proportional to the density of the imaged material (Hubbell & Seltzer, 2004). X-ray tomography can therefore be employed to estimate bulk material densities (Pedrotti et al., 2005; Petrovic et al., 1982). Neutrons, in contrast, interact most strongly with specific isotopes, among them  $^{10}\text{B}$  and  $^{113}\text{Cd}$  as well as isotopes of rather exotic elements such as gadolinium (Sears, 1992). Neutron cross sections for hydrogen (i.e.,  $^1\text{H}$ ), which is abundant in water and in SOM, are much larger (approximately 20–30 times larger) than cross-sections for isotopes of the most common elements in soil, such as Si, Al and O. In contrast, other elements that are abundant in organic matter, namely carbon and nitrogen, interact less strongly with neutrons than  $^1\text{H}$ , but still 3–5 times stronger than silica and aluminium. Relevant isotopes of iron and manganese with even larger neutron cross-sections (approximately 1/3 of the cross-section for  $^1\text{H}$ ) are present in soil. Common isotopes of lithium and chlorine may potentially contribute to neutron attenuation in soils in arid climates. In soils of humid climates, however, these elements are only present in small concentrations as they are relatively mobile in soil and therefore leached out easily.

Table 1 illustrates that hydrogen has clearly the largest neutron cross-section of the most common elements in soil. Other elements with larger neutron cross-sections that are typically found in soils, albeit in lower abundances, are chloride, manganese and iron. The neutron  $\eta$  ( $\text{cm}^{-1}$ ) and X-ray  $\alpha$  ( $\text{cm}^{-1}$ ) attenuation coefficients of a specific substance, for example, quartz, is calculated from the product of its density and the sum of the abundance-weighted cross-sections of the elements composing the substance. The detailed relationship between neutron attenuation coefficients, cross-sections and neutron wavelengths is given in the material and methods section. Figure 1 depicts the neutron attenuation coefficients for common soil minerals and SOM. The respective molecular formulas and bulk densities are given in Table 2. Figure 1 demonstrates that substances containing boron or cadmium (here represented by borax and cadmium sulphate) attenuate neutrons by an order of magnitude better than water and SOM, which are the most attenuating soil materials that are generally present in larger quantities. The large neutron attenuation of

**TABLE 1** List of elements common in soil. Also shown are their average abundance in soil, their atomic weight and the X-ray  $\sigma_x$  and neutron  $\sigma_n$  cross-sections

Element	Abundance in soil (ppm)	Atomic weight ( $\text{g mol}^{-1}$ )	$\sigma_x$ ( $\text{cm}^2 \text{g}^{-1}$ )	$\sigma_n$ (barn = $10^{-24} \text{cm}^2$ )
H	233,412	1.008	0.33	53.4
B	29	10.811	0.16	1627.8
C	26,118	12.011	0.18	5.7
N	2240	14.007	0.18	15.7
O	480,391	15.999	0.19	4.4
F	165	18.998	0.19	4.1
Na	3411	22.99	0.23	4.8
Mg	3227	24.305	0.26	4.0
Al	41,274	26.982	0.28	2.0
Si	184,296	28.086	0.32	2.3
P	405	30.974	0.35	4.8
S	342	32.065	0.41	2.2
Cl	44	35.453	0.44	88.1
K	5616	39.098	0.57	6.6
Ca	5871	40.078	0.66	3.7
Ti	1638	47.867	0.77	17.4
Mn	286	54.938	1.06	30.3
Fe	11,235	55.845	1.21	16.8
Cd	0.05	112.411	5.98	4208.4

*Note:* The elemental content in soil and the atomic weights were derived from Essington (2003). The data for  $\sigma_x$  corresponds to a photon energy of 60 keV and obtained from Chantler (1995, 2003), while  $\sigma_n$  was calculated for the neutron white beam at the IMAT beamline based on the data published in Brown et al. (2018). The neutron cross-sections were weighted by the natural isotopic composition of each element, whereas only isotopes with natural abundances of more than 1% were considered.

water, SOM, but also gibbsite, is due to their relative large hydrogen (i.e., protium) content. Also the next largest neutron attenuators, the clay minerals, owe this property to the hydrogen present in their crystal structure or associated with them in the form of crystal water. Note that the error bars in Figure 1 show the range of attenuation in dependence on either the degree of saturation with crystal water in cadmium sulphate, borax and clay minerals or the ratio between carbon and hydrogen atoms in SOM (Table 2). Also variations in the density (Table 2) of the minerals or the organic matter were considered here.

It follows that the local organic matter content in soil can be estimated from neutron attenuation images if (i) the local bulk density is known, (ii) the sample is free from water and larger amounts of chloride, (iii) the concentration of isotopes with large neutron cross-sections,

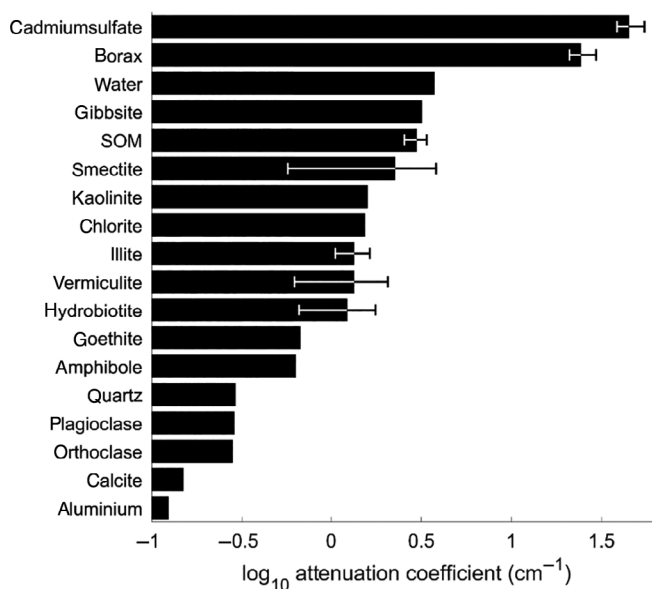


**FIGURE 1** Neutron attenuation coefficients of common soil minerals and organic matter for thermal neutrons

like  $^{10}\text{B}$  and  $^{113}\text{Cd}$  is negligible and (iv) the neutron attenuation related to clay minerals, hydroxides and oxides of iron as well as manganese can be identified. The local bulk density may be estimated from the local X-ray attenuation, as discussed above. Chloride salts, if present in larger concentrations, may be flushed out. The removal of water can be achieved by oven drying. With the exceptions of contaminated soils, both boron and cadmium are trace elements occurring in concentrations low enough to rule out measurable bias in neutron attenuation in soil. In soil of temperate and cold climates, larger concentrations of manganese and iron usually occur in the form of precipitates, which can be identified in X-ray images due to their density contrast. The main challenge is to distinguish between contributions to neutron attenuation of SOM and clay minerals, or, for tropical soils devoid of clay minerals, iron oxides. Albeit that soil minerals are clearly denser than organic matter, the local X-ray attenuation alone is not sufficient to distinguish between effects of porosity, organic materials and specific minerals on the local neutron cross-sections in soil.

A solution to this challenge may be offered by time-of-flight (TOF) neutron imaging available at the IMAT beamline at the ISIS neutron spallation source, Oxfordshire, UK. TOF refers to the individual detection of neutrons travelling at distinct ranges of speed. The neutron travel velocity is deterministically related to their de Broglie wavelength. For thermal neutrons, that is, neutrons with velocities approximately in equilibrium with room temperature (Rinard, 1991), these wavelengths

range mainly between 1 and 9 Å, following a log-normally distributed density function. Neutrons, similar to X-rays, are diffracted at crystal plane spacings. Hence, TOF neutron imaging is able to detect d-spacings, which may be exploited in a similar way as in X-ray diffraction (XRD), a standard method for analysing soil mineral compositions (Harris & White, 2008). In spectra of neutron attenuation for different wavelengths, d-spacings manifest as so-called Bragg edges (Santisteban et al., 2001). Bragg edges are located at twice the respective d-spacing on the neutron spectrum, as the neutron wavelength then becomes too large to be diffracted, which results in a sudden decrease in attenuation. Woracek et al. (2015) have demonstrated that neutron Bragg-edge imaging is able to distinguish between different iron crystal configurations in steel. We are not aware of any attempt to apply TOF neutron imaging on soil. This pilot study evaluates the potential and limitations of joint X-ray and TOF neutron imaging for 3-D mapping local concentrations of minerals and SOM in intact soil. The experiments conducted in this study were carried in the framework of the beamtime documented in Koestel et al. (2019).

## 2 | MATERIAL AND METHODS

### 2.1 | Soil and material properties

In spring 2019, we collected soil samples from the topsoil of four long term field experiments in southern Sweden (Skåne, namely near Borgeby, Ekebo, Fjärdingslöv and Orup) on 25 May 2019 and from two long-term field experiments close to Uppsala in eastern Sweden (Fors and Kungsgängen), on 1 June 2019. All six field sites are part of the soil fertility experiment series R3-9001 of the Swedish University of Agricultural Sciences. The experiments were established between 1957 and 1969. Since the start of the experiments, the sites have been under crop rotations that are typical for the local climatic condition. They have been tilled conventionally. Half of the experimental area was fertilised exclusively with mineral fertilisers, the other half received farmyard manure (FYM) instead or in addition to mineral fertiliser. At each site exists one treatment (two replicates) that had not received any fertiliser for at least 50 years. Over time, lower organic matter contents had established in these plots. In contrast, one treatment per site received a maximum amount of FYM in addition to mineral NPK fertiliser. Here, the organic matter content has increased with time. The difference in SOM between the two treatments and per site is given in Table 3. The mineral composition of the soils at the sampling sites was obtained

**TABLE 2** List of values used in this study for the chemical composition and solid density  $\rho_s$  of soil organic matter and common soil minerals

Substance	Elemental composition	$\rho_s$ (g cm <sup>-3</sup> )	$\eta_{WB}$ (cm <sup>-1</sup> )
Water	H <sub>2</sub> O	1	3.7
SOM	CH <sub>1.15</sub> O <sub>0.49</sub> N <sub>0.06</sub>	1.43 (1.4–1.47)	3 (2.6–3.4)
Wood	CH <sub>1.59</sub> O <sub>0.74</sub>	0.7 (0.43–0.9)	1.6 (1–2)
Quartz	SiO <sub>2</sub>	2.62 (2.6–2.65)	0.3
Plagioclase	Na <sub>0.5</sub> Ca <sub>0.5</sub> Al <sub>1.5</sub> Si <sub>2.5</sub> O <sub>8</sub>	2.675 (2.67–2.69)	0.3
Orthoclase	KAlSi <sub>3</sub> O <sub>8</sub>	2.56	0.3
Amphibole	CaMg <sub>5.5</sub> Al <sub>0.8</sub> Fe <sub>0.1</sub> Si <sub>7</sub> O <sub>24</sub> H <sub>2</sub>	3.22 (2.92–3.52)	0.6
Epidote	Ca <sub>2</sub> Fe <sub>2.25</sub> Al <sub>0.75</sub> Si <sub>3</sub> O <sub>13</sub> H	3.45 (3.3–3.6)	0.6
Kaolinite	Al <sub>2</sub> Si <sub>2</sub> O <sub>9</sub> H <sub>4</sub>	2.6	1.6
Muscovite	KAl <sub>3</sub> Si <sub>3</sub> O <sub>11.8</sub> H <sub>1.8</sub> F <sub>0.2</sub>	2.82 (2.77–2.88)	0.7
Illite	K <sub>0.6</sub> Al <sub>1.3</sub> Mg <sub>0.3</sub> Fe <sub>0.1</sub> Si <sub>3.5</sub> O <sub>11.4</sub> H <sub>3.2</sub> · H <sub>2</sub> O	2.75 (2.6–2.9)	1.3 (1.1–1.6)
Smectite	Na <sub>0.2</sub> Ca <sub>0.1</sub> Al <sub>2</sub> Si <sub>4</sub> O <sub>12</sub> H <sub>2</sub> · 10 H <sub>2</sub> O	2.35 (2–2.7)	2.3 (0.6–3.8)
Vermiculite	Mg <sub>1.8</sub> Fe <sub>0.9</sub> Al <sub>4.3</sub> Si <sub>12</sub> H <sub>2</sub> · 4 H <sub>2</sub> O	2.5 (2.3–2.7)	1.3 (0.6–2.1)
Chlorite	Mg <sub>1.8</sub> Fe <sub>1.6</sub> Mn <sub>1.6</sub> Si <sub>3</sub> Al <sub>2</sub> O <sub>18</sub> H <sub>7.3</sub>	2.97 (2.87–3.07)	1.5
Hydrobiotite	Mg <sub>2.3</sub> Fe <sub>0.6</sub> K <sub>0.3</sub> Ca <sub>0.1</sub> Si <sub>2.8</sub> Al <sub>1.2</sub> O <sub>11.8</sub> H <sub>1.8</sub> F <sub>0.2</sub> · 3 H <sub>2</sub> O	2.56 (2.49–2.64)	1.2 (0.7–1.8)
Hematite	Fe <sub>2</sub> O <sub>3</sub>	5.3	0.9
Goethite	FeO <sub>2</sub> H	3.8 (3.3–4.3)	0.7
Lepidocrocite	FeO <sub>2</sub> H	4	0.7
Boehmite	AlO <sub>2</sub> H	3.03 (3–3.07)	0.3
Gibbsite	AlO <sub>3</sub> H <sub>3</sub>	2.34 (2.3–2.4)	3.2
Calcite	CaCa <sub>3</sub>	2.71	0.1
Anatase	TiO <sub>2</sub>	3.9	0.8
Birnesite	Na <sub>0.3</sub> Ca <sub>0.1</sub> K <sub>0.1</sub> Mn <sub>2</sub> O <sub>4</sub> · 1.5 H <sub>2</sub> O	3	0.8
Apatite	Ca <sub>5</sub> P <sub>3</sub> O <sub>12.33</sub> H <sub>0.33</sub> F <sub>0.33</sub> Cl <sub>0.33</sub>	3.19 (3.16–3.22)	0.5
Borax	Na <sub>2</sub> B <sub>4</sub> O <sub>9</sub> H <sub>4</sub> · 8 H <sub>2</sub> O	1.72 (1.71–1.73)	24.2 (21–30)
Cadmium sulphate	CdSO <sub>4</sub> · H <sub>2</sub> O	3.79 (3.08–4.69)	44.7 (39–55)
Argiletz illite powder	K <sub>0.4</sub> Al <sub>1.5</sub> Mg <sub>0.2</sub> Fe <sub>0.1</sub> Si <sub>3.1</sub> O <sub>10.7</sub> H <sub>3.4</sub> · 1.1 H <sub>2</sub> O	2.65 (2.6–2.7)	1.2
Aluminium	Al	2.7	0.1

Note: Some minerals were not included in any of the samples investigated in our study but added for comparison. The neutron attenuation coefficients  $\eta_{WB}$  were calculated for the white beam at the IMAT beamline using Equation (2). In parenthesis we give considered minimum and maximum values, which are the result of variations of the bulk density, assumed content of crystal water and, in the case of SOM, different assumed H:C ratios.

Abbreviation: SOM, soil organic matter.

from the literature, more specifically from Andrist-Rangel et al. (2013), Kirchmann (1991), Kirchmann and Eriksson (1993) and Kirchmann et al. (1999), and is summarised in Table 4. A collection of literature with more detailed information on the individual sites of the long-term field experiment series is compiled in Luck et al. (2011). In addition to the samples from the long-term field experiments, we used illite clay powder (*Argiletz*, green illite clay, Table 4), apatite and quartz sands as well as sawdust to create composite samples of different mineral composition and known organic matter content.

## 2.2 | Sample preparation

### 2.2.1 | Samples used for the neutron and X-ray radiography as well as XRD

The soil samples from the long-term field experiment were first air-dried for several days in a drying room. Then, larger aggregates were crushed in a mortar and the soil materials were sieved into three different size fractions: <0.125 mm, between 0.125 and 0.63 mm and >0.63 mm in effective diameter. Samples from replicated treatments were not mixed. For each of the two finer

TABLE 3 Texture and organic carbon contents for the soil samples used in this study

Sampling site/material name	Material type	No of samples	Sand (g g <sup>-1</sup> )	Silt (g g <sup>-1</sup> )	Clay (g g <sup>-1</sup> )	SOM (g g <sup>-1</sup> )
Borgeby	Soil	4	0.52	0.25	0.23	0.023–0.024
Ekebo	Soil	3	0.47	0.35	0.18	0.039–0.05
Fjärdingslöv	Soil	2	0.62	0.24	0.14	0.02–0.027
Fors	Soil	2	0.24	0.58	0.18	0.036–0.041
Kungsängen	Soil	2	0.04	0.40	0.56	0.036–0.046
Orup	Soil	2	0.59	0.29	0.12	0.033–0.039
Argiletz illite powder	Single material	3	0	0	1	0
Apatite sand	Single material	2	1	0	0	0
Quartz sand	Single material	1	1	0	0	0
Composite samples	Composite	9	0–0.68	0	0.32–1	0.006–0.1

Note: The texture data for the soil samples were obtained from Kirchmann (1991), for Borgeby and Orup it was Kirchmann and Eriksson (1993) and for Ekebo and Fjärdingslöv it was Kirchmann et al. (1999). The SOM values correspond to the latest data published in the framework of the long-term fertilisation experiment R3-9001 reported on <https://www.slu.se/institutioner/mark-miljo/forskning/vaxtnaringslara-/vaxtnaring/langliggande-vaxtnaringsforsk/r3-9001/> (accessed August 2020). The SOM values correspond to the low and high C treatments, respectively.

fractions, one sample for each of the six sites and two treatments and replicates were packed into small aluminium containers with height 20 and inner width and breadth of 16 and 6 mm, respectively, and a wall thickness of 2 mm. A dry packing procedure was chosen where layers of a few mm of unconsolidated material were added and compacted with a hex key consecutively until the container was filled. The containers were then closed using adhesive aluminium foil. The resulting 48 soil samples exhibited packed dry bulk densities between 0.95 and 1.3 g cm<sup>-3</sup>. In addition, 63 samples were prepared from illite powder, sawdust, quartz sand and apatite sand as well as various mixtures thereof. Composite samples were first mixed prior packing. The samples were packed into the 20 × 16 × 6 mm aluminium containers as described above. The dry bulk densities for these samples varied from approximately 0.6 g cm<sup>-3</sup> for illite powder to 2.2 g cm<sup>-3</sup> for the apatite sand.

Due to time constraints at the neutron beamline, only 30 of all 103 prepared samples could be investigated. These were 15 samples from each of the long-term field experiment sites, two samples with apatite sand, one sample with quartz sand, 2 samples with illite powder and 10 composite samples containing different amounts of illite powder, saw dust and quartz and apatite sand. Among the samples from the long-term field experiment were at least one pair from each of the six sampled sites, one sample from an unfertilised treatment and one from a fertilised treatment. For the sites at Borgeby, Fjärdingslöv, Fors, Kungsängen and Orup, these were samples packed with the fraction <0.125 mm, for Ekebo the fraction 0.125–0.63 mm were investigated. In addition, we measured one sample from Ekebo with the fraction <0.125 mm and two samples from Borgeby filled with the 0.125–0.63 mm

fraction and >0.63 mm fraction. The fine fraction (<0.125 mm) of the soil samples and the illite powder and the apatite sand were also investigated with XRD.

### 2.2.2 | Sample used for neutron and X-ray tomography

A small aluminium column with an inner diameter of 18 mm, a height of 21.3 mm and a wall thickness of 1.65 mm was loosely filled with samples of all materials enumerated above to provide a large variety of different soil materials. Fragments with effective diameters >0.63 mm from fertilised and unfertilised treatments from all six long-term field experiments were included. Additional soil fragments from sampling sites close to Uppsala, among them an aggregate from an organic soil from Helgesta with a SOM content of more than 20%, cucumber and endive seeds, microplastic particles and gravel-sized stones from Ultuna (granite) and Fors (quartz) were included as target objects with different mineral and organic compositions.

## 2.3 | XRD measurements

We conducted XRD measurements on the sieved sample material using a Rigaku Miniflex 600 located at the ISIS materials characterisation lab. The X-ray diffractometer was equipped with a Cu target. The copper K<sub>α</sub>-edge was used to conduct the measurements. Here, we aimed at detecting prominent diffraction peaks that may be visible as Bragg edges in the TOF neutron imaging data. The XRD data also served to characterise the mineral

TABLE 4 Overview of mineral composition of the soils and the illite powder used in this study

Sample type	Quartz (%)	Feldspar (%)	Illite (%)	Smectite (%)	Vermiculite (%)	Chlorite (%)	Kaolinite (%)	Amphibole (%)	Epidote (%)	Other (%)
Borgeby fine	47.3	16.4	18.5	0	7.3	0	5.8	0.3	0.9	3.5
Borgeby coarse	54.2	18.2	12.6	0	5.2	0	6.9	0.4	1.1	1.4
Ekebo fine	43.7	28.2	5.8	11.1	1.4	0.8	2.2	2.2	0.7	3.9
Ekebo coarse	43.9	28.2	5.7	10.9	1.4	0.8	2.2	2.2	0.7	4
Fjärdingslöv	56.1	19.4	8	10.1	2	0.7	0.7	1.5	0.4	1.1
Fors	27.6	23.6	26.2	6.4	0	5.2	5.5	3.9	0	1.6
Kungsängen	10.6	10.6	42.3	24.8	0.4	6.2	2.5	2.1	0	0.5
Orup	38.6	35.5	5.2	0	4.3	0	3.9	1	2.4	9.1
Argiletz illite powder	0	0	70	0	0	0	10	0	0	20

Note: The data for the Kungsängen and Fors soils were obtained from Kirchmann (1991), for Borgeby and Orup it was Kirchmann and Eriksson (1993) and for Ekebo and Fjärdingslöv it was Kirchmann et al. (1999).

composition of the sample material. We corrected the XRD data for bias in the detected diffraction angle by scaling the data to the prominent quartz peaks corresponding to d-spacings of 1.819 and 3.345 Å that were visible in the spectra of all investigated samples except for the apatite sand, for which respective prominent apatite d-spacings were used instead. We evaluated the XRD data by plotting the diffraction signals against the double of corresponding d-spacings to allow a direct comparison with the TOF neutron imaging data. We collected reference XRD data for specific minerals from Lafuente et al. (2015) and www.webmineral.com (accessed January 2021).

## 2.4 | Calculation of theoretical neutron attenuation coefficients

We calculated energy-dependent, effective neutron cross-sections for the elements of relevance for soil using data for all isotopes with more than 1% natural abundance, weighted by abundance. The effective, energy-dependent neutron cross-sections  $\sigma_{e,l}$  (cm<sup>2</sup>) for the individual isotopes were obtained from Brown et al. (2018), where  $\sigma_{e,l} = \sigma_{\text{coh},l} + \sigma_{\text{inc},l} + \sigma_{\text{abs},l}$  with the subscripts indicating contributions from coherent and incoherent scattering as well as from absorption. We computed effective neutron attenuation coefficients  $\hat{\eta}_{i,l}$  (cm<sup>-1</sup>) for the substance  $i$  and wavelength  $l$  by

$$\hat{\eta}_{i,l} = \sum_{e=0}^n \frac{\rho_{s,i} N_a \sigma_{e,l} f_e}{m_e} \quad (1)$$

where  $n$  is the number of different elements in substance  $i$ ,  $\rho_{s,i}$  (g cm<sup>-3</sup>) is the density of the substance,  $N_a$  (mol<sup>-1</sup>) is the Avogadro number,  $\sigma_{e,l}$  is the effective neutron cross-section of element  $e$  at wavelength  $l$ ,  $f_e$  (–) is the mass fraction of element  $e$  in substance  $i$  and  $m_e$  (g mol<sup>-1</sup>) is the standard atomic weight of element  $e$ . Neutron attenuation coefficients for polychromatic neutron beams are easily obtained by the weighted mean of Equation (1) over all neutron wavelengths occurring in the beam. In this fashion, we yielded the theoretical white beam neutron attenuation coefficients  $\hat{\eta}_{i,\text{WB}}$ , for the energy spectrum of the neutron beam used on the IMAT beamline, 2.24–8.06 Å. We computed the neutron attenuation coefficients  $\hat{\eta}_k$  of the soil and the composite samples  $k$  by

$$\hat{\eta}_{k,l} = (1 - \phi_k) \sum_{i=0}^m f_{i,k} \hat{\eta}_{i,l} \quad (2)$$

where  $m$  is the number of substances within a sample,  $f_{i,k}$  (–) is the volume fraction of substance  $i$  in sample  $k$  and

$\phi_k$  ( $\text{cm}^3 \text{cm}^{-3}$ ) is the packed porosity of sample  $k$  calculated as

$$\phi_k = 1 - \frac{\rho_{p,k}}{\rho_{s,k}} \quad (3)$$

with  $\rho_{p,k}$  being the packed bulk density and  $\rho_{s,k}$  the solid phase density of sample  $k$ .

## 2.5 | Image acquisition

### 2.5.1 | Neutron radiography

We recorded 16 neutron radiographs at the IMAT beamline (Burca et al., 2013, 2018) located at the ISIS neutron source within the Rutherford-Appleton Laboratory in Oxfordshire (UK) using the microchannel plate (MCP) detector described in Tremsin et al. (2013) with  $512 \times 512$  pixels each one of  $55 \mu\text{m}$  for an  $L/D$  of 125 (where  $L$  represents the distance between pinhole and detector and  $D$  the pinhole's diameter). We collected data for a wavelength band from 2.24 to  $8.06 \text{ \AA}$ , which was split up into three individual segments by the chosen shutter settings (Tremsin et al., 2014): 2.24–2.9231  $\text{\AA}$ , 2.94–4.9569  $\text{\AA}$  and 4.97–8.06  $\text{\AA}$ . We will refer to the three wavelength segments as ‘shutters 1, 2 and 3’, respectively, in the following. Combining all three shutters, one neutron radiography contained a stack of 2709 images depicting neutron attenuations for the respective individual neutron wavelength. We chose an exposure time of approximately 1 h per radiograph.

Each sample was aligned in a way that the narrow side (10 mm wide) was facing the beam direction. As the field of view of the MCP detector was approximately 30 mm, it was possible to image two material samples in each of the 15 radiographs, totalling in neutron attenuation data for 30 material samples. The 16th radiograph provided information on the brightness distribution of the neutron beam (flat field), which was required to correct for inhomogeneities in the neutron beam and sensitivities of the individual detector pixels.

### 2.5.2 | Neutron tomography

In addition, we collected a 3-D neutron tomography dataset for the cylindrical sample. The data acquisition took place at the IMAT beamline using the setup described in the previous section. Only the exposure time per projection was decreased to approximately 45 min. One hundred forty-two projections were obtained for this sample using a golden-ratio rotation scheme, which

covered rotation angles between 0 and  $180^\circ$ . Five flat-field radiographs were collected prior to the 142 projections and three flat-field radiographs thereafter. The net scan time for the neutron tomography was 4.5 days.

### 2.5.3 | X-ray radiography

We collected X-ray radiographs of all 30 material samples for which we had previously collected neutron radiographs. The images were obtained using a SkyScan 1272 equipped with a Hamamatsu L11871.20 X-ray tube and a Ximea xiRAY11 detector. We used a tube voltage of 90 kV and an electron flux corresponding to  $111 \mu\text{A}$ . The image pixel size was  $6.55 \mu\text{m}$ . Aluminium (0.5 mm) and copper (0.038 mm) sheets were introduced into the beam trajectory to reduce beam hardening.

### 2.5.4 | X-ray tomography

The tomography was performed at the I12-JEEP Beamline at Diamond Light Source (Drakopoulos et al., 2015). The sample was in the same sample holder as during neutron tomography. Two tomography data sets were acquired along the height of the sample because the height of the sample exceeded the vertical field of view, using 55 keV X-rays. For each tomography scan, 1800 projections ( $0$ – $180^\circ$  with  $0.1^\circ$  steps) were recorded with an exposure time of 2.5 ms. The pixel edge length was  $7.91 \mu\text{m}$ , with a field of view ( $H \times V$ ) of  $2560 \times 2160$  pixels or  $22.2 \text{ mm} \times 17.1 \text{ mm}$ .

## 2.6 | Image processing and analyses

### 2.6.1 | Pre-processing of neutron data

We pre-processed the TOF neutron imaging data using the BEAN software (Liptak et al., 2019). In short, we conducted a so-called ‘overlap correction’, which accounts for a systematic underestimation of the neutron counts during high neutron fluxes (Tremsin et al., 2014). We also levelled fluctuations in the neutron beam intensity in between different image projections and scaled the data to a standard neutron flux. To allow for an automatised processing of our projections, we coded the respective parts of the BEAN software into a Matlab script.

Preliminary analyses of the TOF neutron imaging data revealed that the noise level in the image data was too large to allow for the imaging of individual Bragg edges in the 3-D data. We therefore investigated whether an indicator for the soil clay minerals could be detected

by investigating attenuation differences between broader ranges of neutron wavelengths. We achieved this by pooling all image data within each of the three shutters, creating image data for short (shutter 1), medium (shutter 2) and long (shutter 3) neutron wavelengths. In addition, we also investigated the white beam attenuation, which refers to mean attenuation of all 2709 collected wavelengths.

## 2.6.2 | Neutron radiography

The neutron transmission spectra were investigated using the approach documented in Liptak et al. (2019). We applied an edge-preserving filter to reduce the noise in the neutron spectra. More specifically, this was a Savitzky–Golay filter of order 3 and a frame length of 31 values. We then compared the neutron diffraction inherent in the neutron spectra in the form of Bragg edges to d-spacings of common soil minerals and to the XRD spectra collected on the identical sample materials. Under the premise that enough specific crystals are present in a sample (e.g., quartz crystals), Bragg edges manifest in the form of a sudden increase of neutron transmission at wavelengths larger than two times the crystals' d-spacing.

In addition, we investigated the neutron attenuation for the white beam as well as for short, medium and long neutron wavelengths of the 30 imaged samples. This was done to gather means to compare 2-D and 3-D data, as the collected data was too noisy to allow for analysing attenuation data for individual neutron wavelengths. Here, we divided the sample data by the flat field image, which resulted in neutron transmission images. In the optimal case, the resulting image data should range between 0 (no transmission) and 1 (complete transmission, i.e., air). However, we observed slight deviations of a few percentage from 1 when evaluating grey values corresponding to air. Among the reasons for the deviations may be neutron scattering and drifts in the detection efficiency of the detector. In any case, we further corrected the image data by dividing every pixel by the sampled transmission for air. We then defined a second region of interest (ROI) in each radiograph, covering only the grey values corresponding to the sample material (Figure 2a). The neutron transmission  $\tau_{k,n}$  (–) for sample  $k$  was set to the median grey value in this ROI. We calculated the neutron attenuation coefficient  $\eta_k$  ( $\text{cm}^{-1}$ ) using Lambert–Beer's law with

$$\eta_k = -\frac{\ln \frac{\tau_{k,n}}{\exp(-L_{\text{Al}}\eta_{\text{Al}})^2}}{L_s} \quad (4)$$

where  $L_{\text{Al}} = 0.2$  cm is the wall thickness of the aluminium container,  $L_s = 1.6$  cm is the travel distance of the neutron beam through the sample material, and  $\eta_{\text{Al}}$  ( $\text{cm}^{-1}$ ) is the neutron attenuation coefficient for aluminium calculated using Equation (1).

## 2.6.3 | Neutron tomography

We reconstructed a 3-D neutron beam attenuation image for the white beam data as well as for short, medium and long neutron wavelengths. We used the parallel back projection algorithm implemented in the open software *MuhRec* (version 4.2, Kaestner, 2011; Kaestner & Carminati, 2020). In *MuhRec*, we used the 'FullLogNorm' normalisation and modules for the removal and so-called 'spots' and ring-artefacts. The latter is based on Münch et al. (2009).

## 2.6.4 | X-ray radiography

The grey values in the X-ray radiographs were already approximately calibrated to a common greyscale. In the following, we improved the calibration and converted the greyscale to X-ray attenuation images scaling from 0 to 1. For each image, we first sampled grey values in ROIs corresponding to air, aluminium and the sample material (Figure 2b). We then identified the histogram peak in each ROI, which then served as the reference value for the respective material. The X-ray transmission  $\tau_{k,x}$  (–) was then calculated by

$$\tau_{k,x} = \frac{(\gamma_{k,s} - \gamma_{k,\text{Al}})(\bar{\gamma}_{\text{air}} - \bar{\gamma}_{\text{Al}}) + \bar{\gamma}_{\text{Al}}}{\bar{\gamma}_{\text{air}}} \quad (5)$$

where  $\gamma_{k,s}$ ,  $\gamma_{k,\text{air}}$  and  $\gamma_{k,\text{Al}}$  are the grey values of the sample material, the air and the aluminium in sample  $k$  and  $\bar{\gamma}_{\text{air}}$  and  $\bar{\gamma}_{\text{Al}}$  are the arithmetic mean grey values corresponding to air and aluminium of all 30 samples. Note that we assumed the X-ray attenuation in air to be negligible. Finally, we calculated the X-ray attenuation coefficient  $\alpha_k$  of the sample material using Lambert–Beer's law with

$$\alpha_k = -\frac{\ln \frac{\tau_{k,x}}{\exp(-L_{\text{Al}}\alpha_{\text{Al}})^2}}{L_s} \quad (6)$$

where  $\alpha_{\text{Al}}$  is the X-ray attenuation coefficient for aluminium calculated from the image data as

$$\alpha_{Al} = -\frac{\ln \frac{\gamma_{Al}}{\gamma_{air}}}{L_s + 2L_{Al}} \quad (7)$$

### 2.6.5 | X-ray tomography

The tomographic reconstruction was performed using the SAVU system (Wadson & Basham, 2016). A filtered back projection algorithm was used (Ramachandran & Lakshminarayanan, 1971), as implemented in the *ASTRA* toolbox (van Aarle et al., 2015). The top and bottom images of the soil sample were combined into one image with aid of the software *elastix* (Klein et al., 2010; Shamonin et al., 2014), using a rigid registration on the overlapping parts of the two images.

## 2.7 | Registration of 3-D neutron and X-ray images

The X-ray image resolution was first reduced by a factor of approximately 7 to a pixel size of 55  $\mu\text{m}$  to match the nominal resolution of the neutron image. The X-ray and neutron images were then manually aligned by visual inspection. A more precise registration was then carried out using the *elastix* software, which has been shown to allow registration of images from different imaging methods (Lucas et al., 2020; Schlüter et al., 2019). Initially, we conducted a

rigid registration using Mattes' mutual information criterion as objective function to honour the complementary attenuation of X-ray and neutrons. The registration was guided by five visually detected landmarks. Upon the inspection of the registration results, we noticed that the location and alignments of the individual objects in the sample had slightly changed between the neutron and the X-ray scans. This was linked with the need to remove and transport the sample from the IMAT neutron beamline to the I12 synchrotron beamline, where the X-ray image was recorded. To improve the registration results, we conducted a B-spline registration, again using the *elastix* software. The objective function to minimise was composed of the Mattes' mutual information criterion, the Euclidean distance between of 70 visually selected pairs of landmarks in both images and a bending energy constraint term to penalise excessive distortions. The three terms in the objective function were weighted with factors of 1, 0.1 and 20, respectively. A pyramid scheme with three resolution steps (resolution reductions of factors 16, 8 and 4) was used to facilitate the convergence of the registration problem.

## 3 | RESULTS AND DISCUSSION

### 3.1 | Comparison of X-ray and TOF neutron imaging results

Figure 3a,c depict the TOF neutron imaging and XRD spectra for finely sieved (<0.125 mm) soil from the

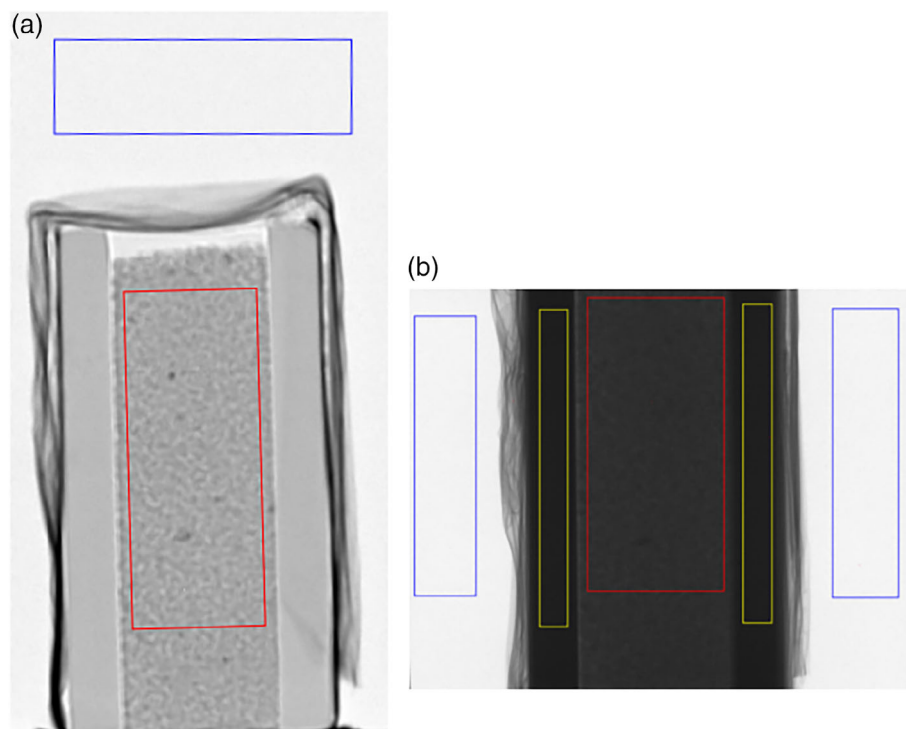


**FIGURE 2** (a) Neutron radiograph of the sample filled with quartz sand and (b) X-ray radiograph of the same sample. The regions of interest (ROIs) from which the grey values of the sample material, the air and the aluminium were obtained are schematically depicted in red, blue and yellow, respectively. Note that the samples were wrapped in adhesive aluminium tape to keep the sample material in place. In (a), the aluminium tape shows up because of the relatively large neutron attenuation of the glue, in (b) it shows up due to the relatively large density of aluminium

Kungsängen site. The XRD data had a much better signal-to-noise ratio, which allowed the detection of several diffraction peaks alongside the most pronounced ones. In the neutron spectrum, only the most prominent diffraction features were distinctively identified in the form of Bragg edges, which were observed at two times the wavelength of the actual d-spacing. These discernable d-spacings are associated with quartz and, to a minor extent, illite (3.34 Å) and aluminium (2.04 Å). The latter is introduced because the samples were stored in aluminium containers during the neutron radiography. As we conducted the XRD measurements directly on the sample material (without aluminium containers), the aluminium diffraction peak is missing in the XRD spectrum. Figure 3b shows the neutron spectrum for quartz sand. The signal-to-noise ratio for this sample was much better, probably because it contained only one mineral instead of a mixture of different minerals like the clay soil from Kungsängen. Moreover, the quartz sand is practically devoid of hydrogen bearing substances like clay minerals or SOM. This causes a twice as large neutron transmission through this sample as through the Kungsängen clay, helping to improve the signal-to-noise ratio. When comparing the neutron spectra of Kungsängen soil and quartz sand (Figure 3a,b), the opposite general trend in neutron transmission with wavelength is striking. While it almost steadily decreases for the clay, it rises for the quartz in discreet jumps at the Bragg edges, followed by a decline. The reason for the former is trivial. For a specific sample and in the absence of Bragg edges, neutron attenuation generally increases with decreasing neutron energy, that is, with increasing neutron wavelength. This trend is also visible in the neutron spectrum for the quartz sand, in between the Bragg edges. However, quartz contains so many prominent Bragg edges between 2 and 6.68 Å that the neutron transmission is decreased for wavelengths <6.68 Å.

### 3.2 | Comparison between calculated and measured neutron attenuation coefficients

Figure 4 depicts the forward modelled neutron attenuation values for the investigated samples, as explained in Section 2.4, using mineral compositions and SOM contents shown in Tables 3 and 4. It is clear that the main portion of white beam neutron attenuation in the six investigated soils was likely associated with clay minerals. If the contribution of all clay minerals is combined, this was even true for the soil taken from the Orup site, which contained the smallest amount of clay (Table 3). Next in importance are quartz and SOM. The former does

not exhibit strong attenuation properties (Figure 1) but accounted significantly to the overall attenuation because of its large abundance in the soil sand and silt fractions. According to the forward modelling, SOM made up between approximately 8% and 20% of the neutron attenuation, depending on its own concentration and the amount of clay minerals in the soil (Figure 4, Tables 3 and 4). In other words, the relative contrast provided by SOM in a neutron image is increasingly diminished with clay content.

Given the limited data on the material composition of the 30 investigated radiography samples available for this study, the measured and predicted neutron attenuation coefficients matched reasonably well (Figure 5). We overestimated the white beam neutron attenuation for the soils from Kungsängen and Fors. This mismatch may be related to uncertainties in soil texture, clay mineralogy, organic matter content and the amount of crystal water still present in the samples. In the calculations, we had assumed that 50% of the crystal water was still present in the clay minerals despite oven drying at 105°C. Reducing the amount of crystal water for these samples by approximately 50% would lead to better matches with the measured values. The overestimation in white beam neutron attenuation of the composite samples containing quartz (all overestimated composite samples in Figure 5) as well as the quartz sample itself can be explained by the effect of the Bragg edges, which was not considered in the calculations. The computed white beam neutron attenuation of the other composite samples matched well with the measured values. To achieve a good match for the samples containing sawdust, we adjusted the neutron cross-section of the sawdust to four times the theoretical value for wood. Probably, the sawdust contained borates, which are commonly used flame retardants on wood products. Borates contain boron, which has a large neutron cross-section. Finally, the white beam neutron attenuations in the Fjärdingslöv and Ekebo samples were clearly underestimated adopting our calculations. Again, uncertainties in soil texture, mineral contents, organic matter content and crystal water contents may explain the deviation.

In summary, detailed characterisations of the mineralogy and organic matter are necessary to predict the neutron attenuation coefficients of soil. Taking the mismatch between measured and calculated neutron attenuation of the 15 composite samples as a standard, we calculated a root mean squared error of 0.028 cm<sup>-1</sup>, corresponding to a measurement precision of approximately 10%. This value is an overestimation, since the scattering effects on the quartz crystal were not considered and the information on the mineral composition of the Argiletz illite powder and the apatite sand we had at our disposal was only approximate.

### 3.3 | Using neutron and X-ray attenuation to infer to material properties in soil

When all 30 radiography samples were considered, measured X-ray attenuation coefficients  $\alpha$  were indeed very well correlated with the sample bulk densities  $\rho_p$  (Figure 6a). A linear regression between  $\alpha$  and  $\rho_p$  resulted in a coefficient of determination of 0.93. In principal, the correlation between X-ray attenuation and clay content may be related as clay soils have commonly a larger porosity than soils of coarser textures. In our study, the strong negative correlation between packed bulk density and clay content was aided by practical difficulties to pack the Argiletz illite powder to larger bulk densities. How much this was the case is shown in Figure 6b, where only the 15 soil samples among the 30 radiography samples were included. Here, the significant correlation between X-ray attenuation

and clay content subsides, and similar the correlation between bulk density and clay content. When only soil samples were employed, the coefficient of determination of the linear regression between  $\alpha$  and  $\rho_p$  was reduced to modest 0.6.

More importantly, a comparison between Figure 6a,b reveals that the neutron attenuation was only significantly correlated with the organic matter content when all 30 samples were included but not when only the soil samples were considered. Among the 30 radiography samples, there were five samples containing no organic matter, and three of them did not contain clay minerals. All five samples had very low neutron attenuation coefficients. These samples introduced a contrast in organic matter contents required for the significant correlation. At the same time, they masked the significant correlation between neutron attenuation and clay content in samples with relatively constant organic matter contents, namely the 15 soil samples (SOM approximately between 2 and

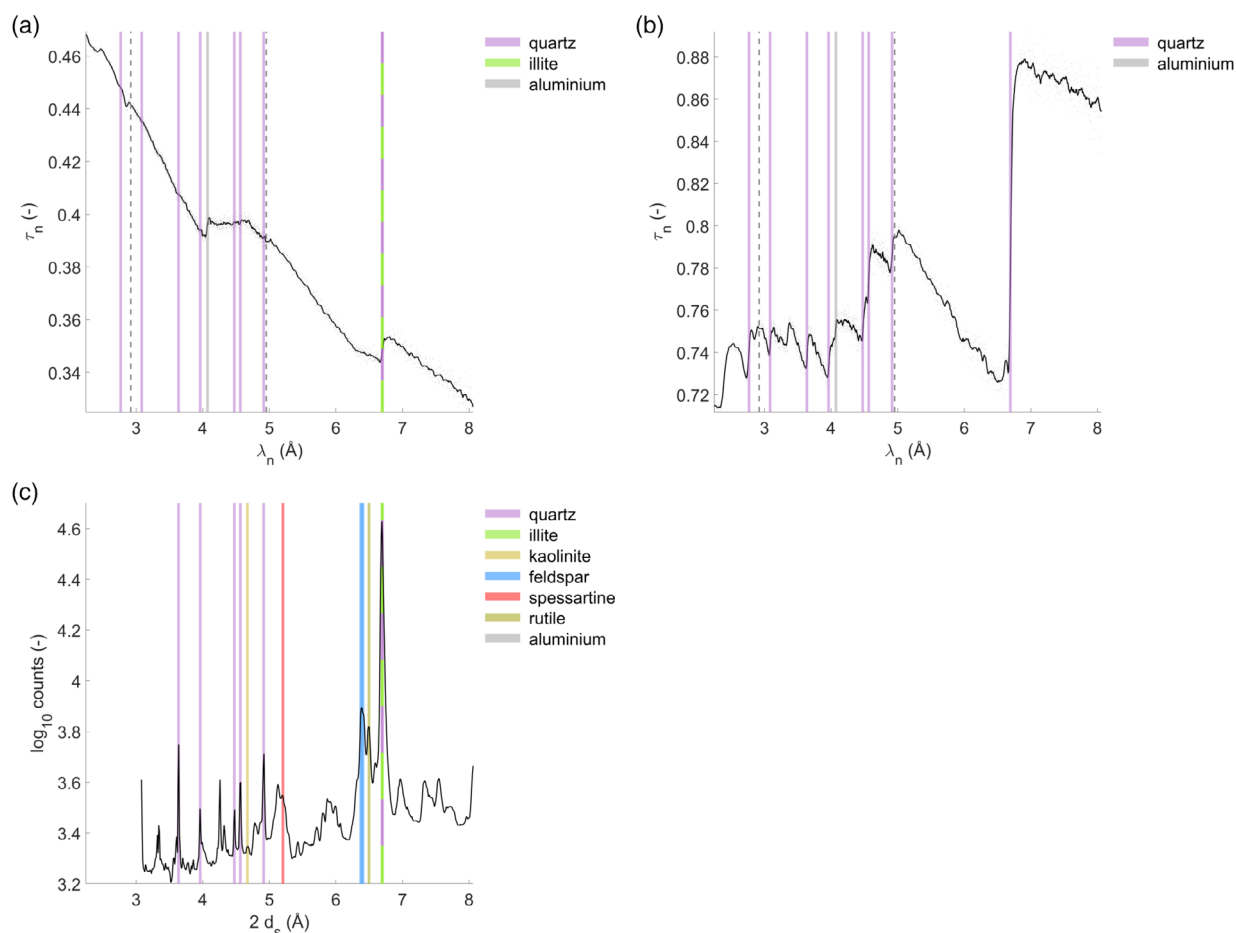


**FIGURE 3** (a) Neutron transmission  $\tau_n$  spectrum for neutron wavelength  $\lambda_n$  for sieved (<0.125 mm) soil from the Kungsängen site, (b) the neutron transmission spectrum for quartz sand and (c) the X-ray diffraction (XRD) spectrum for the sieved (<0.125 mm) soil from the Kungsängen site. The XRD spectrum is plotted against two times the d-spacings  $d_s$ , to facilitate a comparison with the neutron data. Prominent d-spacings are illustrated with different colours

5 wt%). It follows that white beam neutron attenuation may provide a reasonable prediction for organic matter contents in soils with large local variations in organic matter but not in varying clay content. Or, the other way around, white beam neutron attenuation may be used to estimate local clay contents in soils with no organic matter or no spatial variations in organic matter. In other words, it is not feasible to distinguish between clay and organic matter contents using combined neutron and X-ray attenuation measurements when mixtures of these constituents are present. As a result, inference to voxel scale SOM concentrations is presently not feasible.

Information on the attenuation of neutrons with different wavelength cannot resolve this issue (Figure 6).

Other than the soil matrix with unknown clay and organic matter contents, combined neutron and X-ray imaging is more useful to characterise material properties of objects that are larger than the detector pixel size, such as sand grains, seeds or plastics. Figure 7 illustrates the different attenuation coefficients for one vertical cross-section through the investigated 3-D sample. While seeds and plastic beads located in the vertical middle of the sample strongly attenuated neutrons (Figure 7a), they barely diminished the X-ray (Figure 7b). In contrast, the

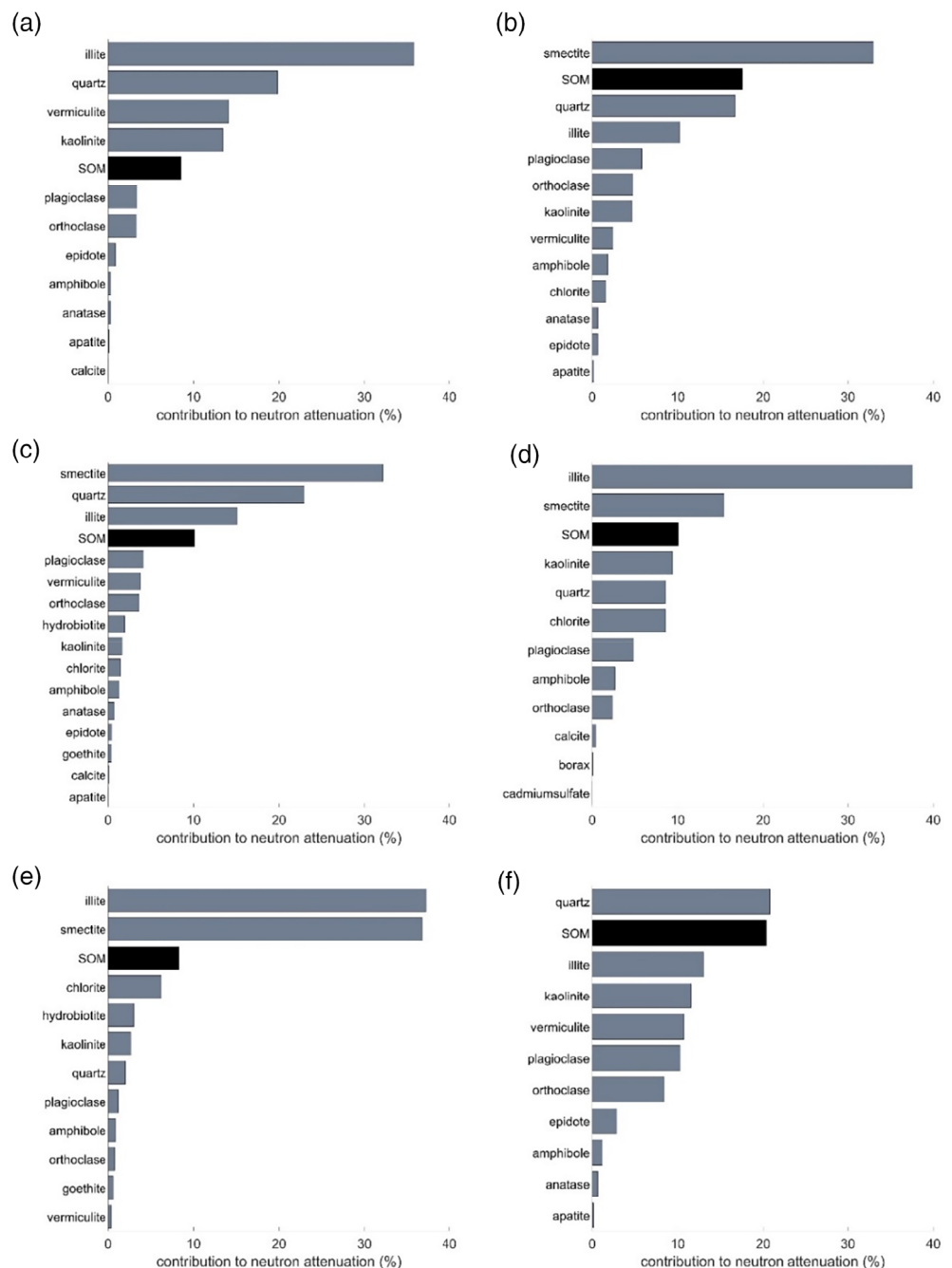


**FIGURE 4** The expected contribution to the neutron attenuation of different minerals and organic matter in dry soil for the topsoils from the six long-term field sites. The neutron attenuation was forward modelled based on the mineral composition and soil organic matter (SOM) content listed in Tables 3 and 4, using the molecular formulas from Table 2. A content of 50% of the maximally possible crystal water was assumed. The panels correspond to (a) Borgeby, (b) Ekebo, (c) Fjärdingslöv, (d) Fors, (e) Kungsängen, and (f) Orup. In panel (d), also the contribution of boron and cadmium for typical concentrations for Swedish soil is indicated as equivalents of borax and cadmium sulphate

X-ray attenuation coefficients are the strongest for the apatite sand in the bottom of the samples and individual mineral phases within gravel grains and soil aggregates. The object in the upper left corner of Figure 7 corresponds to a pebble that attenuates both, neutrons and X-ray relatively well, hinting to a dense material with a relatively large neutron cross-section, most likely containing iron.

Figure 8 shows the two-dimensional histogram of neutron and X-ray attenuation. In Figure 8, some individual peaks on the histogram are labelled with

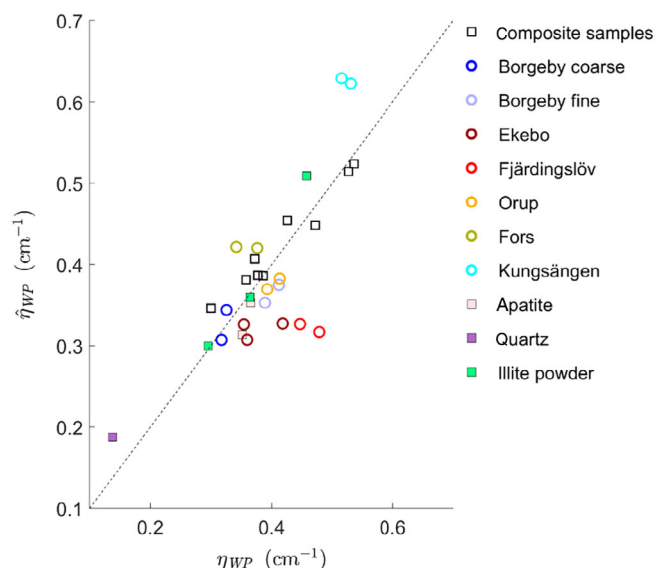


**FIGURE 5** White beam neutron attenuation coefficients measured at the neutron beam at IMAT,  $\eta_{WB}$  ( $\text{cm}^{-1}$ ), versus calculated attenuation coefficients,  $\hat{\eta}_{WB}$  ( $\text{cm}^{-1}$ )

abbreviations for the materials with the corresponding attenuation properties. The histogram illustrates that combined white-beam neutron and X-ray attenuations may serve to distinguish between seeds and plastics. Also distinctions between different kinds of seeds and plastics should be feasible. The former is demonstrated by the image data collected in this study, which shows smaller neutron attenuation for cucumber than for endive seeds. The latter follows from the fact that some plastics differ in their content of hydrogen atoms (e.g., polystyrene with one and polyethylene with two hydrogen per carbon atoms) while others differ in their density (e.g., polyethylene:  $0.92 \text{ g cm}^{-3}$  and polyvinylchloride:  $1.38 \text{ g cm}^{-3}$ ). In addition, minerals in sand and gravel grains containing heavy metal elements may be well characterised (Figures 7 and 8). From Figure 8, it becomes obvious that it is only possible to distinguish between different soil samples when the soil contains either extreme contents of organic matter (Helgesta), clay minerals (Kungsängen) or a sufficiently different bulk density (Helgesta and Orup).

In addition, quartz sand may be identified by exploiting its strong attenuation for thermal neutrons with short wavelengths. We implemented such an approach in Figure 9, which shows four horizontal cross-sections through the 3-D sample. Three channels are superimposed in this image: the X-ray attenuation as a grey scale, the white beam neutron attenuation as a green-scale and, as the third channel, the difference between long and short wavelength neutron attenuations, that is,  $\eta_3 - \eta_1$ . In the third channel, negative values are depicted in a blue scale and positive in a red scale. Neutral values are colourless. Quartz grains exhibit negative values in the third channel and a relatively strong X-ray

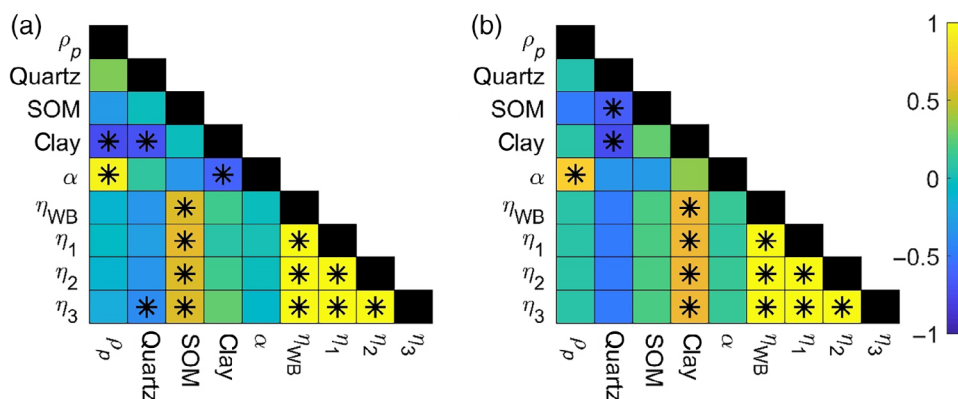


**FIGURE 6** Pearson correlation coefficients for all 30 investigated radiography samples (a) and the 15 soil samples among them (b) between packing bulk density,  $\rho_p$  ( $\text{g cm}^{-3}$ ), quartz content ( $\text{g g}^{-1}$ ), soil organic matter content ( $\text{g g}^{-1}$ ), clay content ( $\text{g g}^{-1}$ ) and attenuation coefficients for X-ray,  $\alpha$  ( $\text{cm}^{-1}$ ), the neutron white beam,  $\eta_{WB}$  ( $\text{cm}^{-1}$ ) and neutrons with short ( $2.24 \leq \lambda_n \leq 2.92 \text{ \AA}$ ), medium ( $2.94 \leq \lambda_n \leq 4.96 \text{ \AA}$ ) and long ( $4.97 \leq \lambda_n \leq 8.06 \text{ \AA}$ ) wavelengths,  $\eta_1$ ,  $\eta_2$ ,  $\eta_3$ , respectively. Asterisks indicate significance at  $p = 0.05$

**FIGURE 7** Vertical cross-sections through the 3-D sample showing white beam neutron (a) and X-ray (b) attenuation coefficients ( $\text{cm}^{-1}$ )

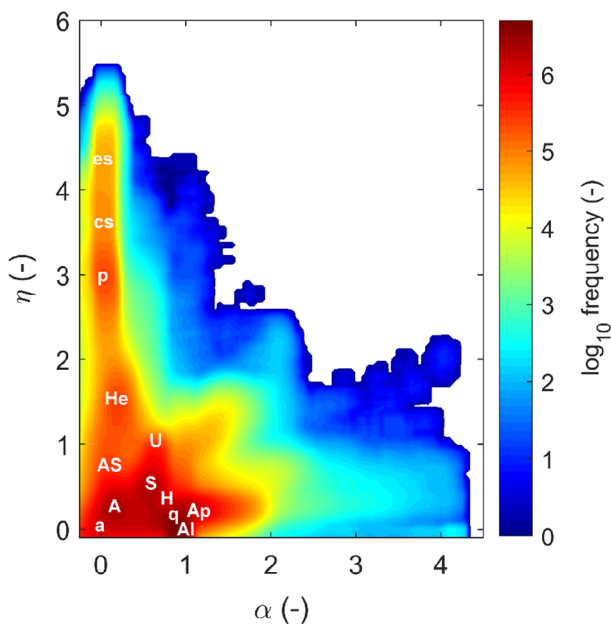
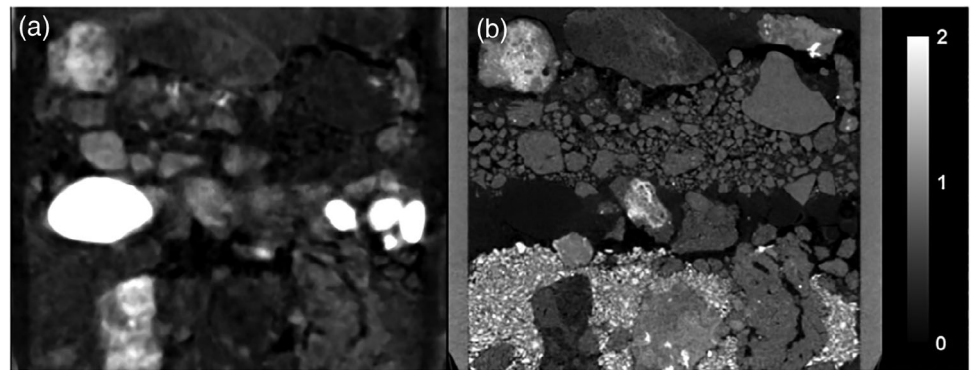


**FIGURE 8** Bi-modal histogram. The x-coordinate shows the X-ray attenuation and the y-coordinate the white-beam neutron attenuation. The hotter the colour, the more image voxels had this combination of X-ray and neutron attenuation values. The letters denote the following materials: a, air; A, Argiletz illite powder; Al, aluminium; Ap, apatite; AS, Argiletz illite powder with 10% sawdust; cs, cucumber seeds; es, endive seeds; H, soil from the Orup site; He, organic soil from the Helgesta site; p, plastics; q, quartz; S, soil from the Borgeby, Ekebo, Fjärdingslöv and Fors sites; U, soil from the Kungsängen site

attenuation. They show up as a whitish blue as seen in Figure 9a,b for the quartz sand. Probably, the mineral phases shown in blue in the gravel grains in Figure 9a,c,d are also quartz. The aluminium sample container wall has a similar signature. Sawdust is shown in green (Figure 9a), as it has strong neutron, minimal X-ray attenuation and equally large attenuation of short and long wavelength neutrons. The minerals in the pebble with large neutron and X-ray attenuation show up in

white (Figure 9a, left side). The Argiletz illite powder is shown in red (Figure 9a,c), due to the large clay content ( $\eta_3 > \eta_1$ ) and low bulk density (small  $\alpha$ ). Plant seeds and plastic beads are shown in yellow (small  $\alpha$ , large  $\eta_{WB}$  and  $\eta_3 > \eta_1$ ), green and cyan (Figure 9c). Greenish colours dominate at the edges of the seeds and beads, while cyan is found for the objects in central positions of the image plane. The dependence on location suggests that these may be imaging artefacts from neutron scattering and beam hardening. Soil aggregates are depicted in a whitish reddish orange due to elevated clay and organic matter contents. Figure 9b shows aggregates from two sites with very different clay and SOM contents: Kungsängen (SOM:  $0.047 \text{ g g}^{-1}$ , clay content:  $0.56 \text{ g g}^{-1}$ ) and Borgeby (SOM:  $0.024 \text{ g g}^{-1}$ , clay content  $0.235 \text{ g g}^{-1}$ ). This allows to visually discern aggregates from either site. Note that within most soil aggregates, clear variations in neutron attenuation are visible, which indicate heterogeneous distributions of clay minerals, SOM or both.

#### 4 | CONCLUSION

Our study demonstrates that a combination of neutron and X-ray imaging is able to identify different materials in soils, provided that they are larger than the detectors' pixel size. Including neutron information contained in the TOF neutron imaging data has the potential to quantify the amount of specific minerals for matrix regions that consists of a mixture of pores, various minerals and SOM. This was illustrated by the clearly identifiable Bragg edges for quartz. However, at present, the poor signal-to-noise ratio of modern TOF neutron technology makes the exploitation of this information for 3-D image data challenging. To increase the signal-to-noise ratio sufficiently to target individual Bragg edges, the image acquisition times for a single sample would need to be increased to several weeks. Advanced noise reduction and signal extraction techniques may offer alternatives. Such methods are presently investigated in

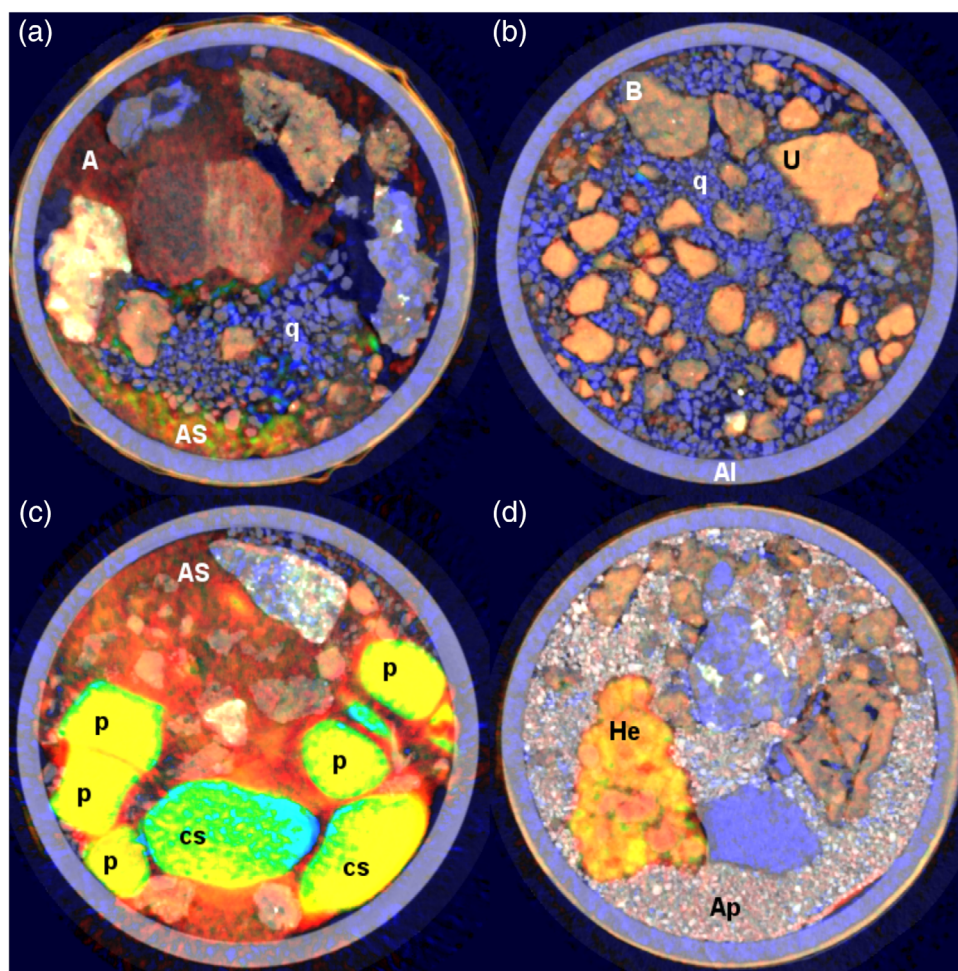


**FIGURE 9** Composite neutron and X-ray images showing 4 different horizontal cross-section through the 3-D sample. The X-ray attenuation is shown in greyscale, the white beam neutron attenuation in a green-scale and the difference between long and short wave neutron attenuation in a blue-black-red colour scale as in Figure 7c. Blue colours indicate stronger attenuation of short than long neutron wavelengths (as is the case for quartz and aluminium), red colours the opposite (as is the case for clay). Yellow, green and cyan colours indicate materials with strong neutron but weak X-ray attenuation. Dark colours indicate low X-ray and neutron attenuation. Light blue colours indicate high X-ray attenuation. The letters denote the following materials: A, Argiletz illite powder; Al, aluminium; Ap, apatite; AS, Argiletz illite powder with 10% sawdust; B, soil from the Borgeby site; cs, cucumber seeds; He, organic soil from the Helgesta site; p, plastics; q, quartz; U, soil from the Kungsängen site

a related study. In the present study, we have shown that the TOF neutron imaging information can identify quartz when the attenuation of neutrons with long and short wavelengths is compared.

The aim of our study was to identify the potential and limitations when mapping organic matter in soils at the voxel scale. The approach presented here turned out to be unsuitable for this task, since it was not possible to distinguish between organic matter and clay minerals in matrix regions, with unknown porosity and where SOM and clay are mixed in unknown ratios. The TOF information was of little use because SOM is highly diverse and therefore lacks clear diffraction edges with which it could be identified. Clay minerals, in contrast, do exhibit d-spacings that are within the main wavelength

range of thermal neutrons. However, these are too weak to serve as means for clay mineral detection in 3-D neutron images. The strongest d-spacings are located between 10 and 20 Å, and their detection require a neutron beam with 4 to 5 times longer wavelengths than those commonly produced at neutron sources. The neutron imaging instrument ODIN (Strobl, 2015) from the European Spallation Source, which is presently built near Lund (Sweden), will be a major development step towards this requirement, as it will allow measuring d-spacings as large as 10 Å. We expect that a voxel-scale identification of SOM and clay contents will become available in next-generation neutron sources. Until then, alternative strategies are needed to map SOM at the voxel scale.

## ACKNOWLEDGEMENTS

We thank Ali Moazzami for providing D2O for a pre-experiment, Yariv Cohen for providing the apatite sand, Michal Snehota for the Quartz sand, Magnus Simonsson for sharing soil samples, Gunnar Börjesson for supplying sawdust and providing access to the field sites of the Swedish long-term fertilisation experiment R3-9001. We would like to thank Gavin Stenning for granting us access to the Rigaku Miniflex 600 in the Materials Characterisation Laboratory at the ISIS Neutron and Muon Source and Dr Chris Spindloe from CLF (Target Fabrication Group) for granting us access to SkyScan 1272 machine for collecting X-ray radiographies. The neutron imaging beamline grant (RB1910494) was provided by STFC ISIS Facility (Koestel et al., 2019). The 3-D X-ray image was acquired during beamtime allocation CM22974-2.

## AUTHOR CONTRIBUTIONS

**John Koestel:** Conceptualisation (lead); data curation (lead); formal analysis (lead); investigation (lead); methodology (lead); project administration (lead); resources (equal); validation (lead); visualisation (lead); writing-original draft (lead); writing – review and editing (lead). **Jumpei Fukumasu:** Investigation (supporting); writing – review and editing (supporting). **Mats Larsbo:** Investigation (supporting); resources (equal); writing – review and editing (supporting). **Anke Herrmann:** Investigation (supporting); resources (supporting); writing – review and editing (supporting). **Pawala Ariyathilaka:** Resources (supporting). **Oxana V. Magdysyuk:** Methodology (supporting); resources (lead); visualisation (supporting); writing – review and editing (supporting). **Genoveva Burca:** Methodology (supporting); resources (lead); visualisation (supporting); writing – review and editing (supporting).

## DATA AVAILABILITY STATEMENT

The data that support the findings of this study are available from the corresponding author upon reasonable request.

## ORCID

John Koestel  <https://orcid.org/0000-0002-3230-5699>

Jumpei Fukumasu  <https://orcid.org/0000-0002-4875-1941>

Genoveva Burca  <https://orcid.org/0000-0001-6867-9628>

## REFERENCES

- Andrist-Rangel, Y., Simonsson, M., Oborn, I., & Hillier, S. (2013). Acid-extractable potassium in agricultural soils: Source minerals assessed by differential and quantitative X-ray diffraction. *Journal of Plant Nutrition and Soil Science*, 176, 407–419.
- Arai, M., Uramoto, G. I., Asano, M., Uematsu, K., Uesugi, K., Takeuchi, A., Morono, Y., & Wagai, R. (2019). An improved method to identify osmium-stained organic matter within soil aggregate structure by electron microscopy and synchrotron X-ray micro-computed tomography. *Soil and Tillage Research*, 191, 275–281.
- Baveye, P. C., Otten, W., Kravchenko, A., Balseiro-Romero, M., Beckers, E., Chalhoub, M., Darnault, C., Eickhorst, T., Garnier, P., Hapca, S., Kiranyaz, S., Monga, O., Mueller, C. W., Nunan, N., Pot, V., Schluter, S., Schmidt, H., & Vogel, H. J. (2018). Emergent properties of microbial activity in heterogeneous soil microenvironments: Different research approaches are slowly converging, yet major challenges remain. *Frontiers in Microbiology*, 9, 1–48.
- Brown, D. A., Chadwick, M. B., Capote, R., Kahler, A. C., Trkov, A., Herman, M. W., Sonzogni, A. A., Danon, Y., Carlson, A. D., Dunn, M., Smith, D. L., Hale, G. M., Arbanas, G., Arcilla, R., Bates, C. R., Beck, B., Becker, B., Brown, F., Casperson, R. J., ... Zhu, Y. (2018). ENDF/B-VIII.0: The 8th major release of the nuclear reaction data library with CIELO-project cross sections, new standards and thermal scattering data. *Nuclear Data Sheets*, 148, 1–142.
- Burca, G., Kockelmann, W., James, J. A., & Fitzpatrick, M. E. (2013). Modelling of an imaging beamline at the ISIS pulsed neutron source. *Journal of Instrumentation*, 8, P10001.
- Burca, G., Nagella, S., Clark, T., Tasev, D., Rahman, I. A., Garwood, R. J., Spencer, A. R. T., Turner, M. J., & Kelleher, J. F. (2018). Exploring the potential of neutron imaging for life sciences on IMAT. *Journal of Microscopy*, 272, 242–247.
- Chantler, C. T. (1995). Theoretical form factor, attenuation, and scattering tabulation for Z=1–92 from E=1–10 eV to E=0.4–1.0 MeV. *Journal of Physical and Chemical Reference Data*, 24, 71–643.
- Chantler, C. T. (2003). Atomic form factors and photoelectric absorption cross-sections near absorption edges in the soft X-ray region. *AIP Conference Proceedings*, 652, 370–377.
- Cnudde, V., & Boone, M. N. (2013). High-resolution X-ray computed tomography in geosciences: A review of the current technology and applications. *Earth-Science Reviews*, 123, 1–17.
- Drakopoulos, M., Connolley, T., Reinhard, C., Atwood, R., Magdysyuk, O., Vo, N., Hart, M., Connor, L., Humphreys, B., Howell, G., Davies, S., Hill, T., Wilkin, G., Pedersen, U., Foster, A., De Maio, N., Basham, M., Yuan, F., & Wanelik, K. (2015). I12: The joint engineering, environment and processing (JEEP) beamline at diamond light. *Journal of Synchrotron Radiation*, 3, 828–838.
- Eickhorst, T., & Tippkötter, R. (2008). Improved detection of soil microorganisms using fluorescence in situ hybridization (FISH) and catalyzed reporter deposition (CARD-FISH). *Soil Biology and Biochemistry*, 40, 1883–1891.
- Essington, M. E. (2003). *Soil and water chemistry: An integrative approach*. CRC Press.
- Harris, W., & White, G. N. (2008). X-ray diffraction techniques for soil mineral identification. In A.L. Ulery & R. Drees (Eds.), *Mineralogical methods* (Vol. 5, pp. 81–115). Methods of soil analysis.
- Herrmann, A. M., Ritz, K., Nunan, N., Clode, P. L., Pett-Ridge, J., Kilburn, M. R., Murphy, D. V., O'Donnell, A. G., & Stockdale, E. A. (2007). Nano-scale secondary ion mass

- spectrometry - A new analytical tool in biogeochemistry and soil ecology: A review article. *Soil Biology & Biochemistry*, 39, 1835–1850.
- Hubbell, J. H., & Seltzer, S. M. (2004). Tables of X-ray mass attenuation coefficients and mass energy-absorption coefficients (version 1.4). In *NIST standard reference database*. National Institute of Standards and Technology (NIST).
- Kaestner, A. P. (2011). MuhRec—A new tomography reconstructor. *Nuclear Instruments and Methods in Physics Research Section A: Accelerators, Spectrometers, Detectors and Associated Equipment*, 651(1), 156–160.
- Kaestner, A. P. & Carminati, C. (2020). MuhRec - version 4.2. Zenodo. <https://doi.org/10.5281/zenodo.3661110>.
- Kaestner, A. P., Hovind, J., Boillat, P., Muehlebach, C., Carminati, C., Zarebanadkouki, M., & Lehmann, E. H. (2017). Bimodal imaging at ICON using neutrons and X-rays, *Physics Procedia* (Vol. 88, pp. 314–321).
- Kirchmann, H. (1991). Properties and classification of soils of the Swedish long-term fertility experiments. *Acta Agriculturae Scandinavica*, 41, 227–242.
- Kirchmann, H., & Eriksson, J. (1993). Properties and classification of soils of the Swedish long-term fertility experiments II. Sites at Örja and Orup. *Acta Agriculturae Scandinavica Section B: Soil and Plant Science*, 43, 193–205.
- Kirchmann, H., Eriksson, J., & Snäll, S. (1999). Properties and classification of soils of the Swedish long-term fertility experiments: IV. Sites at Ekebo and Fjärdingslöv. *Acta Agriculturae Scandinavica Section B: Soil and Plant Science*, 49, 25–38.
- Klein, S., Staring, M., Murphy, K., Viergever, M. A., & Pluim, J. P. (2010). Elastix: A toolbox for intensity-based medical image registration. *IEEE Transactions on Medical Imaging*, 29, 196–205.
- Koestel, J. (2018). SoilJ: An ImageJ plugin for the semiautomatic processing of three-dimensional X-ray images of soils. *Vadose Zone Journal*, 17.1–7.
- Koestel, J., Larsbo, M., Simonsson, M., Fukumasu, J., Herrmann, A. M., & Burca, G. (2019). *Quantitative imaging of the 3-D distribution of organic carbon in naturally structured soil using joint neutron and X-ray imaging*. STFC ISIS Neutron and Muon Source.
- Kravchenko, A. N., Guber, A. K., Razavi, B. S., Koestel, J., Blagodatskaya, E. V., & Kuzyakov, Y. (2019). Spatial patterns of extracellular enzymes: Combining X-ray computed microtomography and 2D zymography. *Soil Biology and Biochemistry*, 135, 411–419.
- Lafuente, B., Downs, R. T., Yang, H., & Stone, N. (2015). The power of databases: The RRUFF project. In T. Armbruster & R. M. Danisi (Eds.), *Highlights in mineralogical crystallography* (pp. 1–30). W. De Gruyter.
- Liptak, A., Burca, G., Kelleher, J., Ovtchinnikov, E., Maresca, J., & Horner, A. (2019). Developments towards Bragg edge imaging on the IMAT beamline at the ISIS pulsed neutron and muon source: BEAN software. *Journal of Physics Communications*, 3(11), 113002.
- Lucas, M., Pihlap, E., Steffens, M., Vetterlein, D., & Kögel-Knabner, I. (2020). Combination of imaging infrared spectroscopy and X-ray computed microtomography for the investigation of bio- and physicochemical processes in structured soils. *Frontiers in Environmental Science*, 8, 42.
- Luck, E., Ruehlmann, J., & Kirchmann, H. (2011). Properties of soils from the Swedish long-term fertility experiments: VI. Mapping soil electrical conductivity with different geophysical methods. *Acta Agriculturae Scandinavica Section B Soil and Plant Science*, 61, 438–447.
- Münch, B., Trtik, P., Marone, F., & Stampanoni, M. (2009). Stripe and ring artifact removal with combined wavelet — Fourier filtering. *Optics Express*, 17, 8567–8591.
- Nunan, N., Schmidt, H., & Raynaud, X. (2020). The ecology of heterogeneity: Soil bacterial communities and C dynamics. *Philosophical Transactions of the Royal Society B*, 375(1798), 20190249.
- Pedrotti, A., Pauletto, E. A., Crestana, S., Holanda, F. S. R., Cruvinel, P. E., & Vaz, C. M. P. (2005). Evaluation of bulk density of Albaqualf soil under different tillage systems using the volumetric ring and computerized tomography methods. *Soil & Tillage Research*, 80, 115–123.
- Peth, S., Chenu, C., Leblond, N., Mordhorst, A., Garnier, P., Nunan, N., Pot, V., Ogurreck, M., & Beckmann, F. (2014). Localization of soil organic matter in soil aggregates using synchrotron-based X-ray microtomography. *Soil Biology and Biochemistry*, 78, 189–194.
- Petrovic, A. M., Siebert, J. E., & Rieke, P. E. (1982). Soil bulk-density analysis in 3 dimensions by computed tomographic scanning. *Soil Science Society of America Journal*, 46, 445–450.
- Ramachandran, G. N., & Lakshminarayanan, A. V. (1971). Three-dimensional reconstruction from radiographs and electron micrographs: Application of convolutions instead of Fourier transforms. *Proceedings of the National Academy of Sciences of the United States of America*, 68, 2236–2240.
- Rawlins, B. G., Wragg, J., Reinhard, C., Atwood, R. C., Houston, A., Lark, R. M., & Rudolph, S. (2016). Three-dimensional soil organic matter distribution, accessibility and microbial respiration in macroaggregates using osmium staining and synchrotron X-ray computed tomography. *The Soil*, 2, 659–671.
- Rinard, P. (1991). Neutron interactions with matter. In D. Reilly, N. Ensslin, & H. J. Smith (Eds.), *Passive nondestructive assay of nuclear materials*. Office of Nuclear Regulatory Research, US Nuclear Regulatory Commission.
- Santisteban, J., Edwards, L., Steuwer, A., & Withers, P. (2001). Time-of-flight neutron transmission diffraction. *Journal of Applied Crystallography*, 34, 289–297.
- Schlüter, S., Eickhorst, T., & Mueller, C. W. (2019). Correlative imaging reveals holistic view of soil microenvironments. *Environmental Science and Technology*, 53, 829–837.
- Sears, V. F. (1992). Neutron scattering lengths and cross sections. *Neutron News*, 3, 26–37.
- Shamonin, D., Bron, E., Lelieveldt, B., Smits, M., Klein, S., & Staring, M. (2014). Fast parallel image registration on CPU and GPU for diagnostic classification of Alzheimer's disease. *Frontiers in Neuroinformatics*, 7, 50.
- Spohn, M., Carminati, A., & Kuzyakov, Y. (2013). Soil zymography—A novel *in situ* method for mapping distribution of enzyme activity in soil. *Soil Biology and Biochemistry*, 58, 275–280.
- Strobl, M. (2015). The scope of the imaging instrument project ODIN at ESS. *Physics Procedia*, 69, 18–26.
- Tremsin, A. S., Vallerger, J. V., McPhate, J. B., & Siegmund, O. H. W. (2014). Optimization of Timepix count rate

- capabilities for the applications with a periodic input signal. *Journal of Instrumentation*, 9, C05026.
- Tremsin, A. S., Vallerger, J. V., McPhate, J. B., Siegmund, O. H. W., & Raffanti, R. (2013). High resolution photon counting with MCP-timepix quad parallel readout operating at > 1 KHz frame rates. *IEEE Transactions on Nuclear Science*, 60, 578–585.
- van Aarle, W., Palenstijn, W. J., De Beenhouwer, J., Altantzis, T., Bals, S., Batenburg, K. J., & Sijbers, J. (2015). The ASTRA toolbox: A platform for advanced algorithm development in electron tomography. *Ultramicroscopy*, 157, 35–47.
- Wadson, N., & Basham, M. (2016). Savu: A python-based, MPI framework for simultaneous processing of multiple, N-dimensional, large tomography datasets. *arXiv*, abs/1610.08015.
- Wildenschild, D., & Sheppard, A. P. (2013). X-ray imaging and analysis techniques for quantifying pore-scale structure and processes in subsurface porous medium systems. *Advances in Water Resources*, 51, 217–246.
- Woracek, R., Penumadu, D., Kardjilov, N., Hilger, A., Boin, M., Banhart, J., & Manke, I. (2015). Neutron Bragg edge tomography for phase mapping. *Physics Procedia*, 69, 227–236.
- Zheng, H., Kim, K., Kravchenko, A., Rivers, M., & Guber, A. (2020). Testing Os staining approach for visualizing soil organic matter patterns in intact samples via X-ray dual-energy tomography scanning. *Environmental Science & Technology*, 54, 8980–8989.

**How to cite this article:** Koestel, J., Fukumasu, J., Larsbo, M., Herrmann, A. M., Ariyathilaka, P., Magdysyuk, O. V., & Burca, G. (2022). Potential of combined neutron and X-ray imaging to quantify local carbon contents in soil. *European Journal of Soil Science*, 73(1), e13178. <https://doi.org/10.1111/ejss.13178>